

# $^{18}\text{O}/^{17}\text{O}$ abundance ratio toward a sample of massive star forming regions with parallax distances

Chao Ou,<sup>1</sup> Junzhi Wang,<sup>1\*</sup> Siqi Zheng,<sup>2</sup> Juan Li,<sup>2</sup> Donatella Romano,<sup>3</sup> Zhi-Yu Zhang<sup>4,5</sup>

<sup>1</sup>Guangxi Key Laboratory for Relativistic Astrophysics, Department of Physics, Guangxi University, Nanning 530004, PR China

<sup>2</sup>Shanghai Astronomical Observatory, Chinese Academy of Sciences, Shanghai, 200030, PR China

<sup>3</sup>INAF, Osservatorio di Astrofisica e Scienza dello Spazio, Via Gobetti 93/3, 40129, Bologna, Italy

<sup>4</sup>School of Astronomy and Space Science, Nanjing University, Nanjing, 210023, PR China

<sup>5</sup>Key Laboratory of Modern Astronomy and Astrophysics (Nanjing University), Ministry of Education, Nanjing 210023, PR of China

Accepted XXX. Received YYY; in original form ZZZ

## ABSTRACT

The  $^{18}\text{O}/^{17}\text{O}$  abundance ratio is, in principle, a powerful tool to estimate the relative contributions of massive stars and low- to intermediate-mass stars to the chemical enrichment of galaxies. We present  $^{18}\text{O}/^{17}\text{O}$  ratios derived from simultaneous observations of  $\text{C}^{18}\text{O}$  and  $\text{C}^{17}\text{O}$  1-0 toward fifty-one massive star forming regions with the Institut de Radioastronomie Millimétrique (IRAM) 30 meter telescope. Simultaneous observations of  $\text{HC}^{18}\text{O}^+$  1-0 and  $\text{HC}^{17}\text{O}^+$  1-0 with the Yebes 40m telescope toward five sources from this sample were also done to test the consistency of  $^{18}\text{O}/^{17}\text{O}$  ratios derived from different isotopic pairs. From our improved measurements, resulting in smaller errors than previous work in the literature, we obtain a clear trend of increasing  $^{18}\text{O}/^{17}\text{O}$  ratio with increasing galactocentric distance ( $D_{GC}$ ), which provides a significant constraint on Galactic chemical evolution (GCE) models. Current GCE models have to be improved in order to explain the observed  $\text{C}^{18}\text{O}/\text{C}^{17}\text{O}$  1-0 gradient.

**Key words:** Stars: evolution – Galaxy: abundances – Galaxy: evolution – ISM: abundances

## 1 INTRODUCTION

Galactic chemical evolution (GCE) models are useful tools to understand the evolution of stars and galaxies (Tinsley 1980; Pagel 1997; Matteucci 2021). These can be exploited to explore the distribution of chemical elements in galaxies and their formation in stars (Matteucci 2021). The interstellar medium (ISM) is often used to study how chemical enrichment proceeds in galaxies (Wilson & Rood 1994). The primary chemical components of the ISM, carbon, nitrogen, and oxygen (CNO), are produced in stars (Burbidge et al. 1957; Wallerstein et al. 1997). The triple- $\alpha$  capture process produce  $^{12}\text{C}$  and then  $^{18}\text{O}$  is synthesised from  $^{14}\text{N}$  seeds during He burning in stars (Salpeter 1952; Clayton 2007), while  $^{13}\text{C}$ ,  $^{15}\text{N}$  and  $^{17}\text{O}$  are produced in H-burning zones via the cold or hot CNO cycles (see Wiescher et al. 2010; see also Romano 2022, for a review of the nucleosynthesis of CNO in stars). Stars release their nucleosynthetic products in the surrounding medium at different phases of the evolution, including the asymptotic giant branch (AGB), supernova phase, etc. (see, e.g., Nomoto, Kobayashi, & Tominaga 2013; Di Criscienzo et al. 2016; Woosley 2019).

Measuring isotope abundance ratios is an efficient method for tracking different stellar nucleosynthesis pathways and putting strong constraints to GCE models (Romano et al. 2017, 2019; Maiolino & Mannucci 2019; Matteucci 2021). Stars of different initial mass and chemical composition, produce isotopes of different species in different amounts on different time scales (Tinsley

1979). The  $^{12}\text{C}/^{13}\text{C}$  ratio, for example, is the result of contributions from stars of different mass that contribute to the existing radial gradient in the Milky Way on different time scales (Milam et al. 2005; Yan et al. 2019). The  $^{14}\text{N}/^{15}\text{N}$  ratio can also be used to study stellar nucleosynthesis and enrichment processes in the ISM (Ritchey, Federman, & Lambert 2015; Colzi et al. 2022).

The  $^{18}\text{O}/^{17}\text{O}$  ratio is, in principle, a useful tracer of stellar nucleosynthesis and metal enrichment processes (Henkel et al. 1994; Wilson & Rood 1994). Oxygen isotopes arrive at the surface of a star through convective motions and are eventually ejected in the ISM, unless further nuclear burnings do not destroy them.  $^{18}\text{O}$  is mainly released by massive stars with initial mass in the range 13–25  $M_{\odot}$  (Romano 2022, and references therein), while  $^{17}\text{O}$  originates from both low- and intermediate-mass stars (Henkel & Mauersberger 1993; Boothroyd & Sackmann 1999). The latter isotope can also be produced in non-negligible quantities during nova outbursts (Romano 2022, and references therein). As a result,  $^{17}\text{O}$  is injected into the ISM on longer time scales slower than  $^{18}\text{O}$ . If the Milky Way is forming inside-out (e.g., Pilkington et al. 2012, and references therein), the  $^{18}\text{O}/^{17}\text{O}$  ratio can decrease over time and display a positive gradient with the galactocentric distance ( $D_{GC}$ ).

The abundance ratios of  $^{18}\text{O}$  to  $^{17}\text{O}$  can be derived from the intensity ratio of  $\text{C}^{18}\text{O}$  and  $\text{C}^{17}\text{O}$  lines (Wouterloot et al. 2008; Zhang et al. 2015; Li et al. 2016; Zhang et al. 2020). The intensity ratio of  $\text{C}^{18}\text{O}/\text{C}^{17}\text{O}$  lines can be viewed as its molecule abundance ratio, given that they have similar excitation properties and are normally optically thin (Wouterloot et al. 2008). The abundance ratio of  $^{18}\text{O}/^{17}\text{O}$  is then obtained from the abundance ratio of  $\text{C}^{18}\text{O}/\text{C}^{17}\text{O}$

\* E-mail: junzhiwang@gxu.edu.cn

as these exhibit similar chemical properties. In the end, the chemical fractionation of oxygen should be negligible because of the high first ionization potential that results in a low abundance of ionized oxygen and barely proceeds the charge exchange reactions (Langer et al. 1984; Loison et al. 2019). The isotope-selective photodissociation effect, which is caused by ultraviolet (UV) radiation, does not considerably alter the abundance ratio of  $C^{18}O/C^{17}O$  because of self-shielding (Bally & Langer 1982; Visser, van Dishoeck, & Black 2009).

The  $^{18}O/^{17}O$  ratio takes a value of  $2.8 \pm 0.2$  in the local ISM, which is smaller than the Solar system value of 5.5 (Wilson, Langer, & Goldsmith 1981). Penzias (1981) measured the ratios of  $^{18}O/^{17}O$  in giant molecular clouds ranging from the Galactic center to  $D_{GC} = 12$  kpc and concluded that the ratio has a uniform value of  $\sim 3.5$ , with variations well within 5%. Wouterloot et al. (2008) instead noted a radial gradient by measuring  $2.88 \pm 0.11$  for the central region,  $4.16 \pm 0.09$  in the galactocentric distance range 4–11 kpc and  $5.03 \pm 0.46$  for the outer Galaxy (16–17 kpc) resting on a sample of 18 sources. Li et al. (2016) measured the ratio for 13 sources covering a galactocentric distance range of 3 kpc to 16 kpc and arrived at a similar conclusion. Finally, Zhang et al. (2020) observed 286 molecular clouds in the galactic disk and determined a gradient of  $^{18}O/^{17}O = (0.10 \pm 0.03) D_{GC} + (2.95 \pm 0.30)$  with an unweighted least-square linear fit to the data. Furthermore, they compared the results with predictions of a GCE model (Romano et al. 2019) thus confirming the existence of a radial gradient. Though Zhang et al. (2020) used a large sample to derive the  $^{18}O/^{17}O$  ratio, the large uncertainties of their observations for individual sources prevented a definite conclusion and limited their use as GCE model constraints.

In this publication, we present the ratios of  $^{18}O/^{17}O$  derived from the intensity ratios of  $C^{18}O/C^{17}O$  1-0 observed with the IRAM 30 m telescope toward fifty-one molecular clouds in the galactocentric distance range 0.2–16 kpc. For five of these sources, the  $^{18}O/^{17}O$  ratios were derived from  $HC^{18}O^+/HC^{17}O^+$  1-0 data taken with the Yebes 40 m telescope. The observations with IRAM 30 m and Yebes 40 m are described in Section 2. The main results are described in Section 3. Sections 4 and 5 follow with the discussion and our conclusions.

## 2 OBSERVATIONS AND DATA REDUCTION

### 2.1 IRAM 30 m observation

We selected fifty-one late stage massive star forming regions with parallactic distances from Reid et al. (2014, 2019). The spectral lines, including  $C^{17}O$  J=1-0 at 112358.988 MHz,  $C^{18}O$  J=1-0 at 109782.176 MHz and  $HC_3N$  J=12-11 at 109173.638 MHz, were observed by using 30 meter millimeter telescope of the Institut de Radioastronomie Millimétrique (IRAM) on Pico Veleta Spain on June and October 2016, and August 2017, which were the same as that presented in Li et al. (2022) for  $NH_2D$  molecules in these sources, while G211.59+01.05 was observed in 2020. The 3 mm (E0) band of The Eight Mixer Receiver (EMIR) and the Fourier Transform Spectrometers (FTS) backend were adopted to cover an 8 GHz bandwidth, with a spectral resolution of 195 kHz and dual polarization. The frequency coverage ranges from 105.8 to 113.6 GHz for the 3mm band (E0). The standard position switching mode with an azimuth offset of  $\sim 600$  arcsec was used.

The IRAM 30-m telescope has a beam size of 22.4 arcsec at 110 GHz. The typical system temperature is about 150 K. Every two

hours, strong nearby quasi-stellar objects were used to correct the pointing offset. Focus was calibrated before each observation or at sunrise and sunset. The main beam bright temperature ( $T_{mb}$ ) is obtained with  $T_{mb} = T_A^* \cdot F_{eff} / B_{eff}$ , where  $T_A^*$  is the antenna temperature, forward efficiency ( $F_{eff}$ ) is 0.93, and the main beam efficiency ( $B_{eff}$ ) is 0.73. Each scan takes 2 minutes observing time, and the total on-source time is 12–234 minutes for each target.

### 2.2 Yebes 40 m observation

For five sources out the total sample, we observed spectral lines of  $HC^{18}O^+$  J=1-0,  $HC^{17}O^+$  J=1-0, and  $HC_3N$  9-8 at rest frequencies of 85162.223, 87057.530, 81881.467 MHz, respectively. The observations were carried out in August 2022 with Yebes 40m telescope, with standard position switching mode. The W-band receiver covers the frequency range of 72–90 GHz with both horizontal and vertical polarizations. The spectral backends are Fast Fourier Spectrometers (FFTs) with 2.5 GHz bandwidths and 38.15 kHz resolution. The spectra are smoothed to 305.2 kHz, corresponding to a velocity resolution of  $1.1 \text{ km s}^{-1}$  at 85 GHz. Pointing corrections were done with SiO  $v=1$  J=2-1 line in VXSGR, V1111OPH, and IRC+00363. The main beam temperature  $T_{mb}$  is obtained with  $T_{mb} = T_A^* / \eta_{mb}$ , where  $\eta_{mb}$  is the main beam efficiency, ranging from 0.30 at 72.5 GHz to 0.21 at 88.5 GHz. The integration time ranged from 2.9 hours to 4.3 hours for different sources, with a typical system temperature of 200 K, which gave an  $1\sigma$  rms noise of 2–6 mK in  $T_A^*$  after averaging the data of both polarizations.

### 2.3 Data reduction

Data reduction is based on the CLASS package in the GILDAS<sup>1</sup> software. The spectra from all sources were averaged by using the CLASS package and then the first-order baseline was removed. The velocity integrated line flux densities were obtained with direct integration of the emission line. The errors of velocity integrated line flux densities were calculated by equation  $\sigma = rms \sqrt{\delta v} \cdot \Delta v$ , where  $\delta v$  was channel separation in velocity and  $\Delta v$  was velocity range for integration, while  $rms$  error was obtained for each spectrum with  $\delta v$  channel spacing. From each spectrum we subtracted a first order baseline and then plotted this on the same velocity scale, as shown in Figure 1(a). All sources were processed and shown in Figure A1, except for G012.80-00.20 and G078.12+03.63 that are displayed in Figure 1.

## 3 RESULTS

$C^{18}O$  J=1-0,  $C^{17}O$  J=1-0 and  $HC_3N$  J=12-11 were detected in all fifty-one sources. Both  $HC^{18}O^+$  1-0 and  $HC^{17}O^+$  1-0 were detected in all five sources. The source names, their aliases and equatorial coordinates were listed in Columns 1–3 of Table 1. The heliocentric distance of each source, which was precisely measured by Reid et al. (2014, 2019) using parallax method, was listed in Columns 4, while  $D_{GC}$  calculated with heliocentric distance of each source was listed in Columns 5. The molecular species and their velocity integrated intensities were listed in Columns 6–7, while the velocity ranges were listed in Columns 8–9. The rms level derived with baseline fitting, the peak temperature, and the central velocity were respectively listed in Columns 10–12, while the latter two were resulted from

<sup>1</sup> <http://www.iram.fr/IRAMFR/GILDAS>

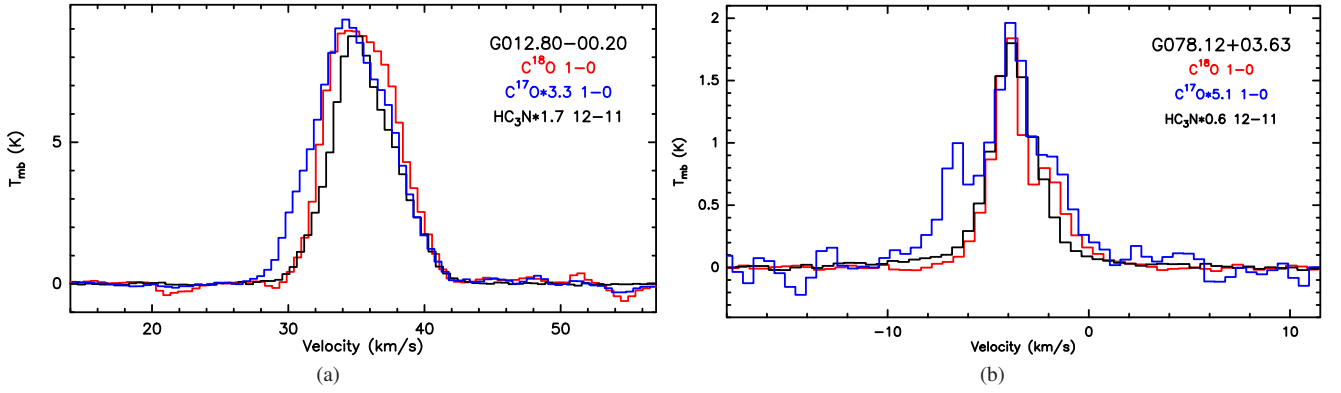


**Figure 1.** The spectra of  $C^{18}O$  1-0,  $C^{17}O$  1-0 and  $HC_3N$  12-11 for two sources as examples. **left:**  $C^{17}O$  1-0 hyperfine structure can not be resolved due to line broadening. **right:** One of the hyperfine can be resolved for source with narrow line width.

Gaussian fitting of the spectra. Column 13 listed the intensity ratio of  $C^{18}O/C^{17}O$  1-0 or  $HC^{18}O^+/HC^{17}O^+$  1-0.

As shown in Table 1, the velocity integrated intensities of  $C^{18}O$  1-0 and  $C^{17}O$  1-0 range from  $2.11 \pm 0.02$  and  $0.53 \pm 0.02$   $K km s^{-1}$  in G183.72-03.66 to  $89.27 \pm 0.26$  and  $30.79 \pm 0.36$   $K km s^{-1}$  in Sgr B2, with mid-value of  $15.10 \pm 0.04$  and  $4.62 \pm 0.06$   $K km s^{-1}$ . The velocity integrated intensities of  $HC^{18}O^+$  1-0 and  $HC^{17}O^+$  1-0 range from  $0.80 \pm 0.03$  to  $3.45 \pm 0.07$   $K km s^{-1}$  and  $0.21 \pm 0.04$  to  $1.03 \pm 0.06$   $K km s^{-1}$ , respectively.

The full width at half maximum (FWHM) of  $C^{18}O$  1-0 and  $C^{17}O$  1-0 lines in our samples were less than  $8 km s^{-1}$ , with the exception of Sgr B2 and W49N. These had FWHMs of approximately 24 and  $14 km s^{-1}$ .  $C^{17}O$  1-0 with obvious hyperfine structure (hfs) features was found in some sources, as shown with blue line in Figure 1(b), which results from the interaction of the electric quadrupole and magnetic dipole moment of the  $^{17}O$  nucleus (Fierking & Langer 1981). The  $C^{17}O$  1-0 spectra exhibited two fairly close components when the FWHM of  $C^{18}O$  1-0 was lower than  $3 km s^{-1}$ , such as G059.78+00.06. Additional velocity component can be found in several sources, such as W49N, due to multiple clouds with different distances in the line of sight. Emission at off positions could result in a fake ‘absorption’ feature, such as in G049.48-00.36. As observations of the two line pairs,  $C^{18}O/C^{17}O$  1-0 and  $HC^{18}O^+/HC^{17}O^+$  1-0, were made simultaneously, the uncertainties of absolute flux calibration did not cause extra error of the line ratio. The ratios of  $C^{18}O/C^{17}O$  were above  $10\sigma$  level for all sources.

The abundance ratios can be derived from the intensity ratios, by multiplying the frequency correction factors of 1.047 derived with  $(\nu_{C^{17}O}/\nu_{C^{18}O})^2$  (e.g., Linke et al. 1977; Zhang et al. 2020). After rectification,  $^{18}O/^{17}O$  ratios with errors were shown in Figure 2(a), taking into account the relationship with  $D_{GC}$ . The ratio of G000.67-00.03 was  $3.04 \pm 0.04$ , which was consistent with the values of  $3.09 \pm 0.10$  and  $3.06 \pm 0.03$  reported in Zhang et al. (2015) and Wouterloot et al. (2008) for Sgr B2. The ratio in W3(OH) was  $3.42 \pm 0.04$ , which was 10% lower than the result of  $3.87 \pm 0.09$  from Wouterloot et al. (2008). The main reason for this difference may be due to the non-gaussian line profiles of  $C^{18}O$  1-0 and  $C^{17}O$  1-0 in W3(OH) (see Figure A1), since Gaussian fitting was used in Wouterloot et al. (2008).

The range of corrected  $^{18}O/^{17}O$  ratios derived from  $C^{18}O/C^{17}O$  1-0 was from  $2.66 \pm 0.02$  in G012.88+00.48 to  $4.45 \pm 0.30$  in G168.06+00.82, while such ratios could be higher than 5 in many sources reported in Zhang et al. (2020), which had large error bars. Extra uncertainties in Zhang et al. (2020) could also be caused by the

observations of  $C^{18}O$  1-0 and  $C^{17}O$  1-0 at different time with ARO 12m. Even though there were almost no overlapping sources in our sample and those in Zhang et al. (2020), most of the high  $^{18}O/^{17}O$  ratios in Zhang et al. (2020) are likely due to the large uncertainties of measurement. Gaussian fitting in Zhang et al. (2020) could also cause uncertainties, since  $C^{17}O$  1-0 can not be simple gaussian profiles due to hfs.

The results of  $HC^{18}O^+$  1-0 and  $HC^{17}O^+$  1-0 of five sources (see Table 1) were also plotted in Figure 2(a) as blue triangles where the ratios increased by the frequency correction factors of 1.045, while the spectra were presented in Figure A2. As mentioned in Section 1, it was thought that the effects of chemical and physical processes do not significantly change the ratio of  $HC^{18}O^+/HC^{17}O^+$  from  $^{18}O/^{17}O$  ratio (e.g., Guelin, Cernicharo, & Linke 1982). The abundance ratios of  $^{18}O/^{17}O$  derived from  $HC^{18}O^+/HC^{17}O^+$  1-0 line ratios are consistent with that derived from  $C^{18}O/C^{17}O$  1-0 ratios within the error bars, except for G010.47+00.02, which was  $3.06 \pm 0.27$  derived from  $HC^{18}O^+/HC^{17}O^+$  1-0 and  $3.77 \pm 0.05$  derived from  $C^{18}O/C^{17}O$  1-0.

$C^{18}O$  and  $C^{17}O$  1-0 lines were assumed to be optically thin for deriving  $C^{18}O/C^{17}O$  abundance ratio. However,  $C^{18}O$  1-0 may be optically thick in some cases (e.g., Bensch et al. 2001; Wouterloot, Brand, & Henkel 2005), which can cause underestimation of  $C^{18}O/C^{17}O$  ratio.  $C^{18}O$  1-0 lines with higher  $T_{mb}$  may have higher optical depths than those with lower  $T_{mb}$ . We marked 21 sources with  $C^{18}O$  1-0 peak  $T_{mb}$  higher than 4 K as cyan squares in Figure 2(a), in which  $^{18}O/^{17}O$  ratios may be under estimated due to the optically thick  $C^{18}O$  1-0. There were three sources, G010.62-00.38 (W31), G012.88+00.48 and G012.80-00.20, with peak  $T_{mb}$  of  $C^{17}O$  1-0 higher than 2 K, which means that  $C^{18}O$  1-0 lines in these three sources are very likely optically thick, which can cause underestimated  $^{18}O/^{17}O$  ratio. However, it is difficult to correct for optical depth effects for  $C^{18}O$  1-0 in these sources. In Figure 2(a), we have marked those sources which may have  $C^{18}O$  1-0 lines that are optically thick.

The relation between derived  $^{18}O/^{17}O$  ratios and  $D_{GC}$  was plotted in Figure 2(a). An unweighted least-squares linear fitting gave the result of  $^{18}O/^{17}O = (0.06 \pm 0.02) D_{GC} + (3.07 \pm 0.11)$ , with Pearson’s correlation coefficient of 0.49. On the other hand, as shown in Figure 2(b), using the heliocentric distance instead of  $D_{GC}$ , there was not any correlation.

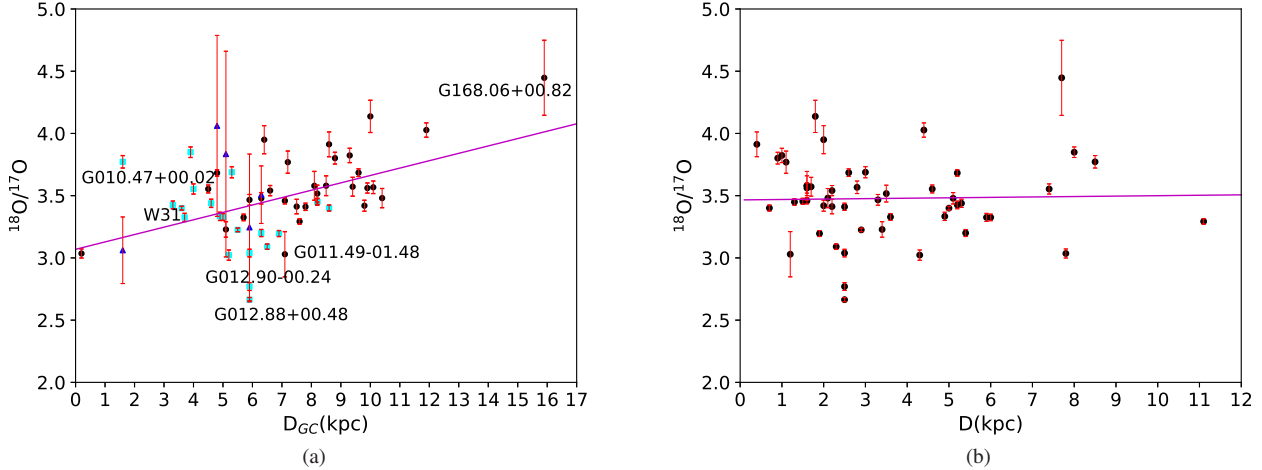


**Figure 2.** The abundance ratio of  $^{18}\text{O}/^{17}\text{O}$  following with the galactocentric distance ( $D_{GC}$ ) on the left and the heliocentric distance on the right. The results from  $\text{HC}^{18}\text{O}^+$  1-0 and  $\text{HC}^{17}\text{O}^+$  1-0 of 5 sources are also shown on the left as blue triangles, while only results from  $\text{C}^{18}\text{O}/\text{C}^{17}\text{O}$  1-0 are on the right. Filled black circles are for sources with  $\text{C}^{18}\text{O}$  1-0 peak  $T_{\text{mb}}$  lower than 4 K, while filled cyan squares for those higher than 4K. The magenta lines are fitting results for data points derived from  $\text{C}^{18}\text{O}/\text{C}^{17}\text{O}$  1-0.

#### 4 DISCUSSION

As shown in Figure 2(a), there is a weak trend of increasing  $^{18}\text{O}/^{17}\text{O}$  ratios with increasing  $D_{GC}$ . A similar trend was previously found with a smaller sample and weak correlation (Wouterloot et al. 2008), or with a relatively large sample but large error bars as well (Zhang et al. 2020). In this work, we provide a much more solid trend.

$^{18}\text{O}$  is synthesised from  $^{14}\text{N}$  seeds during He burning, but can survive successive nuclear burning only in massive stars (Salpeter 1952; Clayton 2007).  $^{17}\text{O}$  is produced in H-burning zones via the cold and hot CNO cycles (Wiescher et al. 2010; Romano 2022), with low- to intermediate-mass stars, massive stars and novae all contributing to its synthesis (e.g., Romano 2022, and references therein). Thus, the  $^{18}\text{O}/^{17}\text{O}$  ratio reflects the relative contributions of massive and low- to intermediate-mass stars, which in turn are related to the star formation history and initial mass function of the system.

Romano et al. (2017) predicted the abundance ratios of CNO isotopes at different times and positions within the Galaxy with their GCE model and compared the results with previous observational data in the literature. Later, Romano et al. (2019) updated the model to include the production of  $^{17}\text{O}$  and  $^{18}\text{O}$  by AGB stars, novae and massive stars including fast massive rotators. The GCE models discussed by Romano et al. (2017, 2019) belong to the class of the two-infall models, where the thick and thin discs of the Milky Way are formed in a sequence out of two distinct episodes of gas accretion. In particular, the thin disc forms from a mixture of gas of primordial chemical composition and enriched gas left over from the previous thick-disc formation process. Zhang et al. (2020) adopted the model results from Romano et al. (2019) to compare with their observational results of  $\text{C}^{18}\text{O}$  and  $\text{C}^{17}\text{O}$  1-0. However, due to the large uncertainties in their individual  $^{18}\text{O}/^{17}\text{O}$  ratio measurements (Zhang et al. 2020), it was hard to provide reliable constraints to the isotope ratios predicted by the GCE model.

Our  $^{18}\text{O}/^{17}\text{O}$  ratios, derived from simultaneous observations of  $\text{C}^{18}\text{O}$  and  $\text{C}^{17}\text{O}$  1-0 in fifty-one sources, are plotted in Figure 3 as a function of  $D_{GC}$ , overlaid to theoretical gradients from five GCE models. The continuous lines refer to the predictions of two-

infall models published in Romano et al. (2019): MWG-10, assuming non-rotating stars and no novae (blue line); MWG-12, assuming fast-rotating stars below  $[\text{Fe}/\text{H}] = -1$  and novae (red line); finally the black line shows MWG-12 without novae. The dashed lines are for models 2 and 4 discussed in Colzi et al. (2022) that are one-infall models referring to the thin disc of the Galaxy. In this case, the thick and thin discs of the Milky Way are formed in parallel out of two distinct episodes of infall of gas of primordial chemical composition (see Grisoni, Spitoni, & Matteucci 2018, for details). At variance with what happens in the case of the two-infall models, the thin disc hence starts with a null metallicity, which allows an important amount of primary  $^{18}\text{O}$  from low-metallicity, massive fast-rotating stars to be ejected in the ISM. None of the models can explain the observational relation between  $^{18}\text{O}/^{17}\text{O}$  ratios and  $D_{GC}$ . The MWG-12 model is closer to the observational results for the inner Galaxy than others, still, profound revisions are required, especially for  $D_{GC}$  between  $\sim 6$  and 11 kpc.

In Figure 3 the scatter at a fixed  $D_{GC}$  is much larger than the observational uncertainties in the data points, which suggests additional factors. The possible underestimation of the  $^{18}\text{O}/^{17}\text{O}$  ratios due to optically thick  $\text{C}^{18}\text{O}$  1-0 (points marked as cyan squares in Figure 2(a)) offers a viable explanation. However, the scatter is still present for the sources marked with filled black circles in Figure 2(a), which are thought to be mainly optically thin for  $\text{C}^{18}\text{O}$  1-0. So, the  $^{18}\text{O}/^{17}\text{O}$  ratio, which is indicative of the ratio of massive stars to low- and intermediate-mass stars, is related not only to  $D_{GC}$ . Since  $^{17}\text{O}$  is synthesised in non-negligible amounts by novae, namely, rare systems characterized by largely variable yields (see Romano et al. 2017, their figure 6), it may well be that part of the scatter is caused by the stochasticity of the enrichment process.

Further simultaneous observations of  $\text{C}^{18}\text{O}$  and  $\text{C}^{17}\text{O}$  1-0 for sources with parallactic distances, such as those in Reid et al. (2019), with high sensitivity so as to secure low uncertainties in the measurements, are necessary to better determine the relation of  $^{18}\text{O}/^{17}\text{O}$  ratio with  $D_{GC}$ . Mapping observations of sources with high  $\text{C}^{18}\text{O}$  1-0 brightness temperature, which may be due to possible optically thick emission, are also needed. Spatially resolved  $\text{C}^{18}\text{O}/\text{C}^{17}\text{O}$  1-0 ratio can be obtained with such mapping observations. With the as-

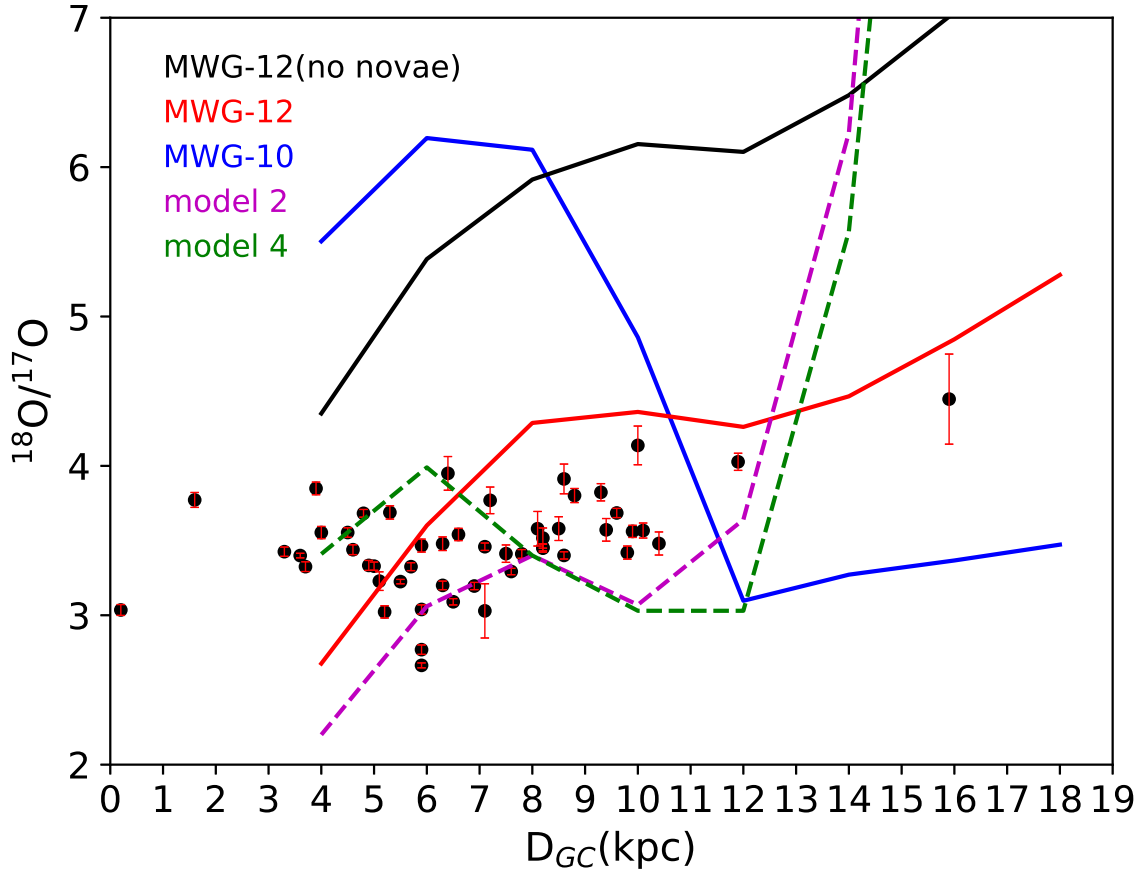


**Figure 3.** The abundance ratio gradient overlaid with GCE model in different condition. Only the ratios obtained from  $C^{18}O$  1-0 and  $C^{17}O$  1-0 are used. The model lines are described in Section 4. The Milky Way galaxy (MWG) and the number indicates the selected yield set combination (see Table 1 in Romano et al. 2019).

sumption of uniform  $^{18}O/^{17}O$  ratio within one source, optically thick  $C^{18}O$  1-0, which should be mainly around the emission peak, might be ruled out, while the  $^{18}O/^{17}O$  ratio can be derived with observational data in the outer regions.  $C^{18}O$  and  $C^{17}O$  2-1 and 3-2 lines can also be used to double check the  $^{18}O/^{17}O$  ratio obtained by  $C^{18}O$  and  $C^{17}O$  1-0 in individual sources, especially for sources with possible optically thick  $C^{18}O$  1-0 emission. Sensitive observations for lines of other molecules, such as  $HC^{18}O^+$  and  $HC^{17}O^+$  1-0, also provide useful supplementary information to check if chemical fractionation is important or not.

## 5 SUMMARY AND CONCLUSION REMARKS

Using observations done with the IRAM 30 meter telescope, we detected  $C^{18}O$  1-0 and  $C^{17}O$  1-0 emission in fifty-one massive star forming regions with accurate distances. The abundance ratio of  $^{18}O/^{17}O$  in each source is obtained from the intensity ratio of  $C^{18}O/C^{17}O$  1-0, both of which are above  $10\sigma$  level in all fifty-one sources.  $^{18}O/^{17}O$  ratio derived with  $C^{18}O$  1-0 and  $C^{17}O$  1-0 has a trend in the radial direction of the Galaxy with  $^{18}O/^{17}O = (0.06 \pm 0.02) D_{GC} + (3.07 \pm 0.11)$ , as obtained from an unweighted least-squares linear fitting with Pearson’s correlation coefficient of

0.49. In contrast, no trend is found for the  $^{18}O/^{17}O$  ratio with the distance from the sun. The relation between  $^{18}O/^{17}O$  ratio and  $D_{GC}$  in these sources is compared to GCE model predictions. Improved GCE models are needed to explain the derived  $^{18}O/^{17}O$  ratio versus  $D_{GC}$  relationship.  $HC^{18}O^+$  1-0 and  $HC^{17}O^+$  1-0 in five of fifty-one sources were also observed with Yebes 40 meter telescope. These provided consistent results of  $^{18}O/^{17}O$  ratios in four sources. However for G010.47+00.02 the  $^{18}O/^{17}O$  ratio obtained with  $HC^{18}O^+$  1-0 and  $HC^{17}O^+$  1-0 observation is lower than that  $C^{18}O$  1-0 and  $C^{17}O$  1-0 measurement.

## ACKNOWLEDGEMENTS

We thank the referee, T.L.Wilson, who provided suggestions for the manuscript. This work is supported by the National Natural Science Foundation of China grant 12173067, 12173016, 12041305, the Program for Innovative Talents, Entrepreneur in Jiangsu and the science research grants from the China Manned Space Project with NOS.CMS-CSST-2021-A08 and CMS-CSST-2021-A07. This work also benefited from the International Space Science Institute (ISSI/ISSI-BJ) in Bern and Beijing, thanks to the funding of the team “Chemical abundances in the ISM: the litmus test of stellar

IMF variations in galaxies across cosmic time” (Principal Investigator Donatella Romano and Zhi-Yu Zhang). This study is based on observations carried out under project number 012-16, 023-17 and 005-20 with the IRAM 30m telescope and on observations carried out with the Yebes 40m telescope. IRAM is supported by INSU/CNRS (France), MPG (Germany) and IGN (Spain). The 40m radio telescope at Yebes Observatory is operated by the Spanish Geographic Institute (IGN; Ministerio de Transportes, Movilidad y Agenda Urbana).

## REFERENCES

- Bally J., Langer W. D., 1982, *ApJ*, 255, 143. doi:10.1086/159812
- Bensch F., Pak I., Wouterloot J. G. A., Klapper G., Winnemisser G., 2001, *ApJL*, 562, L185. doi:10.1086/338253
- Boothroyd A. I., Sackmann I.-J., 1999, *ApJ*, 510, 232. doi:10.1086/306546
- Burbidge E. M., Burbidge G. R., Fowler W. A., Hoyle F., 1957, *RvMP*, 29, 547. doi:10.1103/RevModPhys.29.547
- Choi B.-G., Wasserburg G. J., Huss G. R., 1999, *ApJL*, 522, L133. doi:10.1086/312239
- Clayton D., 2007, *hic.book*
- Colzi L., Romano D., Fontani F., Rivilla V. M., Bizzocchi L., Beltran M. T., Caselli P., et al., 2022, *A&A*, 667, A151. doi:10.1051/0004-6361/202244631
- De Nutte R., Decin L., Olofsson H., Lombaert R., de Koter A., Karakas A., Milam S., et al., 2017, *A&A*, 600, A71. doi:10.1051/0004-6361/201629195
- Di Criscienzo M., Ventura P., García-Hernández D. A., Dell’Aglì F., Castellani M., Marrese P. M., Marinoni S., et al., 2016, *MNRAS*, 462, 395. doi:10.1093/mnras/stw1685
- Frerking M. A., Langer W. D., 1981, *JChPh*, 74, 6990. doi:10.1063/1.441072
- Grisoni V., Spitoni E., Matteucci F., 2018, *MNRAS*, 481, 2570. doi:10.1093/mnras/sty2444
- Guelin M., Cernicharo J., Linke R. A., 1982, *ApJL*, 263, L89. doi:10.1086/183930
- Henkel C., Wilson T. L., Langer N., Chin Y.-N., Mauersberger R., 1994, *LNP*, 72. doi:10.1007/3540586210\_5
- Henkel C., Mauersberger R., 1993, *A&A*, 274, 730
- Langer W. D., Graedel T. E., Frerking M. A., Armentrout P. B., 1984, *ApJ*, 277, 581. doi:10.1086/161730
- Li H.-K., Zhang J.-S., Liu Z.-W., Lu D.-R., Wang M., Wang J., 2016, *RAA*, 16, 47. doi:10.1088/1674-4527/16/3/047
- Li Y., Wang J., Li J., Liu S., Luo Q., 2022, *MNRAS*, 512, 4934. doi:10.1093/mnras/stab3186
- Linke R. A., Goldsmith P. F., Wannier P. G., Wilson R. W., Penzias A. A., 1977, *ApJ*, 214, 50. doi:10.1086/155229
- Loison J.-C., Wakelam V., Gratier P., Hickson K. M., Bacmann A., Agúndez M., Marcelino N., et al., 2019, *MNRAS*, 485, 5777. doi:10.1093/mnras/stz560
- Lugaro M., Liffman K., Ireland T. R., Maddison S. T., 2012, *ApJ*, 759, 51. doi:10.1088/0004-637X/759/1/51
- Maiolino R., Mannucci F., 2019, *A&ARv*, 27, 3. doi:10.1007/s00159-018-0112-2
- Matteucci F., 2021, *A&ARv*, 29, 5. doi:10.1007/s00159-021-00133-8
- Milam S. N., Savage C., Brewster M. A., Ziurys L. M., Wyckoff S., 2005, *ApJ*, 634, 1126. doi:10.1086/497123
- Nomoto K., Kobayashi C., Tominaga N., 2013, *ARA&A*, 51, 457. doi:10.1146/annurev-astro-082812-140956
- Pagel B. E. J., 1997, *nceg.book*, 392
- Penzias A. A., 1981, *ApJ*, 249, 518. doi:10.1086/159311
- Pilkington K., Few C. G., Gibson B. K., Calura F., Michel-Dansac L., Thacker R. J., Mollá M., et al., 2012, *A&A*, 540, A56. doi:10.1051/0004-6361/201117466
- Randich S., Magrini L., 2021, *FrASS*, 8, 6. doi:10.3389/frspas.2021.616201
- Reid M. J., Menten K. M., Brunthaler A., Zheng X. W., Dame T. M., Xu Y., Wu Y., et al., 2014, *ApJ*, 783, 130. doi:10.1088/0004-637X/783/2/130
- Reid M. J., Menten K. M., Brunthaler A., Zheng X. W., Dame T. M., Xu Y., Li J., et al., 2019, *ApJ*, 885, 131. doi:10.3847/1538-4357/ab4a11
- Ritchey A. M., Federman S. R., Lambert D. L., 2015, *ApJL*, 804, L3. doi:10.1088/2041-8205/804/1/L3
- Romano D., Matteucci F., Zhang Z.-Y., Papadopoulos P. P., Ivison R. J., 2017, *MNRAS*, 470, 401. doi:10.1093/mnras/stx1197
- Romano D., 2022, *A&ARv*, 30, 7. doi:10.1007/s00159-022-00144-z
- Romano D., Matteucci F., Zhang Z.-Y., Ivison R. J., Ventura P., 2019, *MNRAS*, 490, 2838. doi:10.1093/mnras/stz2741
- Salpeter E. E., 1952, *ApJ*, 115, 326. doi:10.1086/145546
- Tinsley B. M., 1979, *ApJ*, 229, 1046. doi:10.1086/157039
- Tinsley B. M., 1980, *FCPh*, 5, 287. doi:10.48550/arXiv.2203.02041
- Visser R., van Dishoeck E. F., Black J. H., 2009, *A&A*, 503, 323. doi:10.1051/0004-6361/200912129
- Wallerstein G., Iben I., Parker P., Boesgaard A. M., Hale G. M., Champagne A. E., Barnes C. A., et al., 1997, *RvMP*, 69, 995. doi:10.1103/RevModPhys.69.995
- Wiescher M., Görres J., Uberseder E., Imbriani G., Pignatari M., 2010, *ARNPS*, 60, 381. doi:10.1146/annurev.nucl.012809.104505
- Wilson R. W., Langer W. D., Goldsmith P. F., 1981, *ApJL*, 243, L47. doi:10.1086/183440
- Wilson T. L., Rood R., 1994, *ARA&A*, 32, 191. doi:10.1146/annurev.aa.32.090194.001203
- Wilson T. L., Matteucci F., 1992, *A&ARv*, 4, 1. doi:10.1007/BF00873568
- Woolley S. E., 2019, *ApJ*, 878, 49. doi:10.3847/1538-4357/ab1b41
- Wouterloot J. G. A., Brand J., Henkel C., 2005, *A&A*, 430, 549. doi:10.1051/0004-6361:20040437
- Wouterloot J. G. A., Henkel C., Brand J., Davis G. R., 2008, *A&A*, 487, 237. doi:10.1051/0004-6361:20078156
- Yan Y. T., Zhang J. S., Henkel C., Mufakharov T., Jia L. W., Tang X. D., Wu Y. J., et al., 2019, *ApJ*, 877, 154. doi:10.3847/1538-4357/ab17d6
- Zhang J. S., Liu W., Yan Y. T., Yu H. Z., Liu J. T., Zheng Y. H., Romano D., et al., 2020, *ApJS*, 249, 6. doi:10.3847/1538-4365/ab9112
- Zhang J. S., Sun L. L., Riquelme D., Henkel C., Lu D. R., Zhang Y., Wang J. Z., et al., 2015, *ApJS*, 219, 28. doi:10.1088/0067-0049/219/2/28

Table 1: Data parameters

Source Alias	R.A. (hh:mm:ss)	Decl. (dd:mm:ss)	D (kpc)	$D_{GC}$ (kpc)	Line (1-0)	$\int T_{mb} dv$ (K km s <sup>-1</sup> )	Velocity range (km s <sup>-1</sup> )	Rms (10 <sup>-2</sup> K)	$T_{peak}$ (K)	$V_{LSR}$ (km s <sup>-1</sup> )	Ratio <sub>corr</sub>
G121.29+00.65 L 1287	00:36:47.35	+63:29:02.20	0.9	8.8	$C^{18}O$	7.06(0.01)	-23 -12	0.6	2.51	-17.5(0.1)	3.80(0.05)
					$C^{17}O$	1.95(0.02)	-24 -13	1.0	0.40	-18.1(0.1)	
G123.06-06.30 NGC 281	00:52:24.70	+56:33:50.50	2.8	10.1	$C^{18}O$	5.87(0.02)	-38 -22	0.7	1.62	-30.0(0.1)	3.57(0.05)
					$C^{17}O$	1.72(0.02)	-38 -26	0.9	0.33	-30.7(0.1)	
G133.94+01.06 W 3OH	02:27:03.82	+61:52:25.20	2.0	9.8	$C^{18}O$	15.10(0.04)	-54 -39	1.5	3.28	-47.3(0.1)	3.42(0.04)
					$C^{17}O$	4.62(0.06)	-58 -41	1.9	0.79	-48.0(0.1)	
G168.06+00.82 IRAS 05137+3919	05:17:13.74	+39:22:19.90	7.7	15.9	$C^{18}O$	2.69(0.04)	-29 -21	1.8	1.15	-25.3(0.1)	4.45(0.30)
					$C^{17}O$	0.63(0.04)	-31 -22.4	2.0	0.16	-25.8(0.1)	
G209.00-19.38 Orion Nebula	05:35:15.80	-05:23:14.10	0.4	8.6	$C^{18}O$	3.27(0.02)	3 15	0.6	1.07	8.9(0.1)	3.91(0.10)
					$C^{17}O$	0.88(0.02)	1 18	0.7	0.18	8.4(0.1)	
G176.51+00.20	05:37:52.14	+32:00:03.90	1.0	9.3	$C^{18}O$	4.54(0.02)	-25 -12	0.6	1.83	-17.7(0.1)	3.82(0.06)
					$C^{17}O$	1.24(0.02)	-26 -11	0.7	0.27	-18.2(0.1)	
G183.72-03.66	05:40:24.23	+23:50:54.70	1.8	10.0	$C^{18}O$	2.11(0.02)	-5 10	0.6	0.57	2.3(0.1)	4.14(0.13)
					$C^{17}O$	0.53(0.02)	-4 8	0.6	0.11	1.8(0.1)	
G188.94+00.88 S 252	06:08:53.35	+21:38:28.70	2.1	10.4	$C^{18}O$	4.71(0.02)	-4 10	0.8	1.39	3.2(0.1)	3.48(0.08)
					$C^{17}O$	1.42(0.03)	-5 10	1.1	0.26	2.5(0.1)	
G192.60-00.04 S 255	06:12:54.02	+17:59:23.30	1.6	9.9	$C^{18}O$	7.77(0.02)	1 14	0.8	2.30	7.2(0.1)	3.56(0.04)
					$C^{17}O$	2.28(0.03)	-1 13.5	0.9	0.45	6.8(0.1)	
G211.59+01.05	06:52:45.32	+01:40:23.10	4.4	11.9	$C^{18}O$	3.83(0.01)	40 50	0.4	1.00	45.4(0.1)	4.03(0.06)
					$C^{17}O$	0.99(0.01)	38 49	0.6	0.19	44.8(0.1)	
G232.62+00.99	07:32:09.78	-16:58:12.80	1.7	9.4	$C^{18}O$	5.12(0.03)	6 24	0.8	1.32	16.6(0.1)	3.57(0.08)
					$C^{17}O$	1.50(0.03)	8 23	1.1	0.26	16.0(0.1)	
G000.67-00.03 Sgr B2	17:47:20.00	-28:22:40.00	7.8	0.2	$C^{18}O$	89.27(0.26)	38 110	4.3	3.42	66.9(0.2)	3.04(0.04)
					$C^{17}O$	30.79(0.36)	35 114	5.6	1.22	65.8(0.1)	
G005.88-00.39	18:00:30.31	-24:04:04.50	3.0	5.3	$C^{18}O$	30.56(0.13)	-9 23	3.1	5.96	9.0(0.1)	3.69(0.04)
					$C^{17}O$	8.68(0.10)	-1 17	3.2	1.33	8.3(0.1)	
G009.62+00.19	18:06:15.00	-20:31:31.70	5.2	3.3	$C^{18}O$	38.77(0.07)	-6 16	2.1	6.92	3.7(0.1)	3.43(0.03)
					$C^{17}O$	11.85(0.10)	-6 14	3.2	1.91	3.0(0.1)	
G010.47+00.02	18:08:38.00	-19:51:50.30	8.5	1.6	$C^{18}O$	31.72(0.11)	53 78	3.0	4.56	66.9(0.1)	3.77(0.05)
					$C^{17}O$	8.8(0.11)	57 76	3.6	1.18	66.2(0.1)	
					$HC^{18}O^+$	2.09(0.06)	58 76	1.5	0.32	66.9(0.1)	3.06(0.27)
					$HC^{17}O^+$	0.71(0.06)	58 76	1.3	0.06	65.9(0.1)	
					$C^{18}O$	76.11(0.10)	-14 10	2.7	11.7	-2.8(0.1)	3.40(0.02)
G010.62-00.38 W 31	18:10:28.55	-19:55:48.60	5.0	3.6	$C^{17}O$	23.44(0.10)	-13 7	3.1	3.21	-3.5(0.1)	
					$C^{18}O$	28.73(0.05)	28 39	2.0	8.21	33.3(0.1)	2.66(0.02)
G012.88+00.48 IRAS 18089-1732	18:11:51.42	-17:31:29.00	2.5	5.9	$C^{17}O$	11.29(0.07)	26 39	2.6	2.28	32.7(0.1)	
					$C^{18}O$	10.33(0.06)	33.4 47	2.1	3.16	36.4(0.1)	3.23(0.06)
G011.91-00.61	18:13:58.12	-18:54:20.30	3.4	5.1	$C^{17}O$	3.35(0.06)	30 43	2.4	0.72	36.1(0.1)	
					$HC^{18}O^+$	1.05(0.06)	30 43	1.7	0.28	36.3(0.1)	3.83(0.83)
					$HC^{17}O^+$	0.29(0.06)	30 43	1.6	0.06	36.9(0.1)	
					$C^{18}O$	59.28(0.05)	27 43	1.7	9.52	35.4(0.1)	3.23(0.01)
					$C^{17}O$	19.24(0.09)	26 43	2.9	2.74	34.7(0.1)	
G012.80-00.20	18:14:14.23	-17:55:40.50	2.9	5.5	$C^{18}O$	27.06(0.11)	28 45	3.6	5.98	36.4(0.1)	2.77(0.03)
					$C^{17}O$	10.23(0.11)	28 42	4.0	1.73	35.5(0.1)	
G012.90-00.24	18:14:34.42	-17:51:51.90	2.5	5.9	$C^{18}O$	31.34(0.08)	32 48	2.7	5.82	36.0(0.1)	3.04(0.03)
					$C^{17}O$	10.80(0.11)	28 50	3.1	1.66	35.3(0.1)	
					$HC^{18}O^+$	1.62(0.10)	20 50	1.8	0.46	36.9(0.1)	3.25(0.59)
					$HC^{17}O^+$	0.52(0.09)	20 50	1.6	0.06	37.7(0.1)	
					$C^{18}O$	5.05(0.08)	3 18	2.8	1.22	10.3(0.1)	3.03(0.18)
G014.33-00.64	18:18:54.67	-16:47:50.30	1.1	7.2	$C^{17}O$	1.74(0.10)	1 15.6	3.7	0.27	9.3(0.4)	
					$C^{18}O$	10.70(0.07)	19.7 27	3.3	3.98	22.3(0.1)	3.77(0.09)
G015.03-00.67 M 17	18:20:24.81	-16:11:35.30	2.0	6.4	$C^{17}O$	2.97(0.07)	17.3 25.6	3.3	0.79	22.1(0.1)	
					$C^{18}O$	7.01(0.05)	14 27	1.8	2.03	19.5(0.1)	3.95(0.11)
G016.58-00.05	18:21:09.08	-14:31:48.80	3.6	5.0	$C^{17}O$	1.86(0.05)	13 25	2.1	0.34	19.0(0.1)	
					$C^{18}O$	21.66(0.05)	53 65	2.0	6.44	59.2(0.1)	3.33(0.03)
G023.44-00.18	18:34:39.29	-08:31:25.40	5.9	3.7	$C^{17}O$	6.81(0.05)	51 65	2.0	1.39	58.6(0.1)	
					$C^{18}O$	35.02(0.10)	90 115	2.6	5.98	101.1(0.1)	3.33(0.03)
G023.00-00.41	18:34:40.20	-09:00:37.00	4.6	4.5	$C^{17}O$	11.02(0.10)	90 114	2.9	1.57	100.2(0.1)	
					$C^{18}O$	27.57(0.06)	64 92	1.6	3.43	76.2(0.1)	3.55(0.03)
G027.36-00.16	18:41:51.06	-05:01:43.40	8.0	3.9	$C^{17}O$	8.12(0.07)	63.6 91	1.9	0.93	75.5(0.1)	
					$C^{18}O$	18.88(0.04)	86 98	1.5	4.61	91.2(0.1)	3.85(0.04)
					$C^{17}O$	5.14(0.06)	83 98	2.0	0.98	90.6(0.1)	

Table 1: (continued)

Source Alias	R.A. (hh:mm:ss)	Decl. (dd:mm:ss)	D (kpc)	$D_{GC}$ (kpc)	Line (1-0)	$\int T_{mb} dv$ (K·km s <sup>-1</sup> )	Velocity range (km s <sup>-1</sup> )	Rms (10 <sup>-2</sup> K)	$T_{peak}$ (K)	$V_{LSR}$ (km s <sup>-1</sup> )	Ratio <sub>corr</sub>
G028.86+00.06	18:43:46.22	-03:35:29.60	7.4	4.0	C <sup>18</sup> O	22.21(0.04)	94 110	1.5	5.18	103.2(0.1)	3.55(0.04)
					C <sup>17</sup> O	6.54(0.07)	91 110	2.4	1.02	102.1(0.1)	
G029.95-00.01 W 43S	18:46:03.74	-02:39:22.30	5.3	4.6	C <sup>18</sup> O	28.51(0.06)	90 108	2.1	6.21	97.5(0.1)	3.44(0.03)
					C <sup>17</sup> O	8.68(0.08)	88 108	2.5	1.34	97.0(0.1)	
G031.28+00.06	18:48:12.39	-01:26:30.70	4.3	5.2	C <sup>18</sup> O	21.51(0.06)	100 117	2.0	5.21	109.0(0.1)	3.02(0.04)
					C <sup>17</sup> O	7.45(0.10)	98 115	3.3	1.38	108.3(0.1)	
G031.58+00.07 W 43Main	18:48:41.68	-01:09:59.00	4.9	4.9	C <sup>18</sup> O	19.21(0.06)	87 104	1.8	5.13	96.3(0.1)	3.33(0.03)
					C <sup>17</sup> O	6.03(0.06)	88 102	2.1	1.14	95.7(0.1)	
G032.04+00.05	18:49:36.58	-00:45:46.90	5.2	4.8	C <sup>18</sup> O	17.95(0.04)	86 105	1.2	3.70	95.6(0.1)	3.68(0.03)
					C <sup>17</sup> O	5.10(0.03)	85 104	1.1	0.84	95.0(0.1)	
					HC <sup>18</sup> O <sup>+</sup>	0.80(0.03)	92 102	0.7	0.22	95.4(0.1)	4.06(0.73)
					HC <sup>17</sup> O <sup>+</sup>	0.21(0.04)	92 102	0.8	0.03	96.5(0.1)	
G034.39+00.22	18:53:19.00	+01:24:08.80	1.6	7.1	C <sup>18</sup> O	13.16(0.03)	50 64	1.2	3.06	57.1(0.1)	3.46(0.02)
					C <sup>17</sup> O	3.98(0.03)	50 63	1.0	0.73	56.6(0.1)	
G035.02+00.34	18:54:00.67	+02:01:19.20	2.3	6.5	C <sup>18</sup> O	12.95(0.04)	46 55.8	1.6	4.48	52.4(0.1)	3.09(0.02)
					C <sup>17</sup> O	4.39(0.03)	44 57	1.0	0.92	51.8(0.1)	
G037.43+01.51	18:54:14.35	+04:41:41.70	1.9	6.9	C <sup>18</sup> O	11.68(0.02)	39 49	0.9	4.09	44.2(0.1)	3.20(0.02)
					C <sup>17</sup> O	3.83(0.03)	38 50	1.1	0.79	43.7(0.1)	
G035.19-00.74	18:58:13.05	+01:40:35.70	2.2	6.6	C <sup>18</sup> O	15.98(0.07)	24 44	2.3	3.94	34.0(0.1)	3.54(0.04)
					C <sup>17</sup> O	4.73(0.05)	26 44	1.6	0.84	33.4(0.1)	
G035.20-01.73	19:01:45.54	+01:13:32.50	3.3	5.9	C <sup>18</sup> O	8.51(0.03)	40.4 50	1.3	2.15	44.0(0.2)	3.47(0.04)
					C <sup>17</sup> O	2.57(0.03)	38.5 49	1.3	0.53	43.6(0.1)	
G043.16+00.01 W 49N	19:10:13.41	+09:06:12.80	11.1	7.6	C <sup>18</sup> O	46.06(0.06)	-16 25	1.2	3.23	7.4(0.1)	3.29(0.02)
					C <sup>17</sup> O	14.64(0.09)	-16 30	1.9	0.99	6.6(0.1)	
G043.79-00.12 OH 43.8-0.1	19:11:53.99	+09:35:50.30	6.0	5.7	C <sup>18</sup> O	18.12(0.06)	32 54	1.7	3.01	44.1(0.1)	3.33(0.03)
					C <sup>17</sup> O	5.71(0.04)	31 54	1.2	0.81	43.3(0.1)	
G049.48-00.36 W 51 IRS2	19:23:39.82	+14:31:05.00	5.1	6.3	C <sup>18</sup> O	29.55(0.11)	54 76	3.4	3.70	61.2(0.1)	3.48(0.05)
					C <sup>17</sup> O	8.89(0.11)	53 71	3.6	1.02	60.5(0.1)	
G049.48-00.38 W 51M	19:23:43.87	+14:30:29.50	5.4	6.3	C <sup>18</sup> O	55.92(0.17)	48 74	4.5	6.42	56.2(0.1)	3.20(0.03)
					C <sup>17</sup> O	18.30(0.15)	46 81	3.6	1.89	55.6(0.1)	
					HC <sup>18</sup> O <sup>+</sup>	3.45(0.07)	45 70	1.3	0.37	56.7(0.1)	3.51(0.23)
					HC <sup>17</sup> O <sup>+</sup>	1.03(0.06)	45 70	1.3	0.10	55.9(0.1)	
G059.78+00.06	19:43:11.25	+23:44:03.30	2.2	7.5	C <sup>18</sup> O	6.04(0.03)	16 27	1.1	2.16	22.7(0.1)	3.41(0.06)
					C <sup>17</sup> O	1.85(0.03)	15 30	1.1	0.36	22.1(0.1)	
G069.54-00.97 ON 1	20:10:09.07	+31:31:36.00	2.5	7.8	C <sup>18</sup> O	14.57(0.03)	3 19	1.0	3.59	11.4(0.1)	3.41(0.03)
					C <sup>17</sup> O	4.47(0.04)	2 20	1.2	0.81	10.7(0.1)	
G078.12+03.63 IRAS 20126+4104	20:14:26.07	+41:13:32.70	1.6	8.1	C <sup>18</sup> O	5.10(0.03)	-9 4	1.3	1.45	-3.7(0.1)	3.58(0.12)
					C <sup>17</sup> O	1.49(0.05)	-11 2	1.8	0.28	-3.9(0.1)	
G075.76+00.33	20:21:41.09	+37:25:29.30	3.5	8.2	C <sup>18</sup> O	7.39(0.04)	-10 7	1.3	1.72	-1.6(0.1)	3.52(0.07)
					C <sup>17</sup> O	2.20(0.04)	-11 4	1.5	0.38	-2.3(0.1)	
G081.87+00.78 W 75N	20:38:36.43	+42:37:34.80	1.3	8.2	C <sup>18</sup> O	21.18(0.05)	0 20	1.6	5.14	9.7(0.1)	3.45(0.03)
					C <sup>17</sup> O	6.43(0.05)	0 19	1.5	1.12	9.0(0.1)	
G081.75+00.59 DR 21	20:39:01.99	+42:24:59.30	1.5	8.2	C <sup>18</sup> O	13.92(0.03)	-9 -1	1.6	5.68	-4.0(0.1)	3.46(0.02)
					C <sup>17</sup> O	4.22(0.03)	-12 0	1.1	0.92	-4.5(0.1)	
G092.67+03.07	21:09:21.73	+52:22:37.10	1.6	8.5	C <sup>18</sup> O	5.38(0.02)	-11 -2	1.1	2.01	-6.1(0.1)	3.58(0.08)
					C <sup>17</sup> O	1.57(0.03)	-13 -1	1.4	0.35	-6.4(0.1)	
G109.87+02.11 Cep A	22:56:18.10	+62:01:49.50	0.7	8.6	C <sup>18</sup> O	19.14(0.03)	-18 -2	1.0	5.08	-10.7(0.1)	3.40(0.02)
					C <sup>17</sup> O	5.89(0.04)	-21 -2	1.3	1.09	-11.4(0.1)	
G111.54+00.77 NGC 7538	23:13:45.36	+61:28:10.60	2.6	9.6	C <sup>18</sup> O	11.99(0.03)	-68 -45	0.7	2.37	-57.1(0.1)	3.68(0.03)
					C <sup>17</sup> O	3.41(0.03)	-70 -46	0.8	0.55	-57.7(0.1)	



**APPENDIX A: THE SPECTRAL LINES OF ALL SAMPLE**

This paper has been typeset from a  $\text{\TeX}/\text{\LaTeX}$  file prepared by the author.

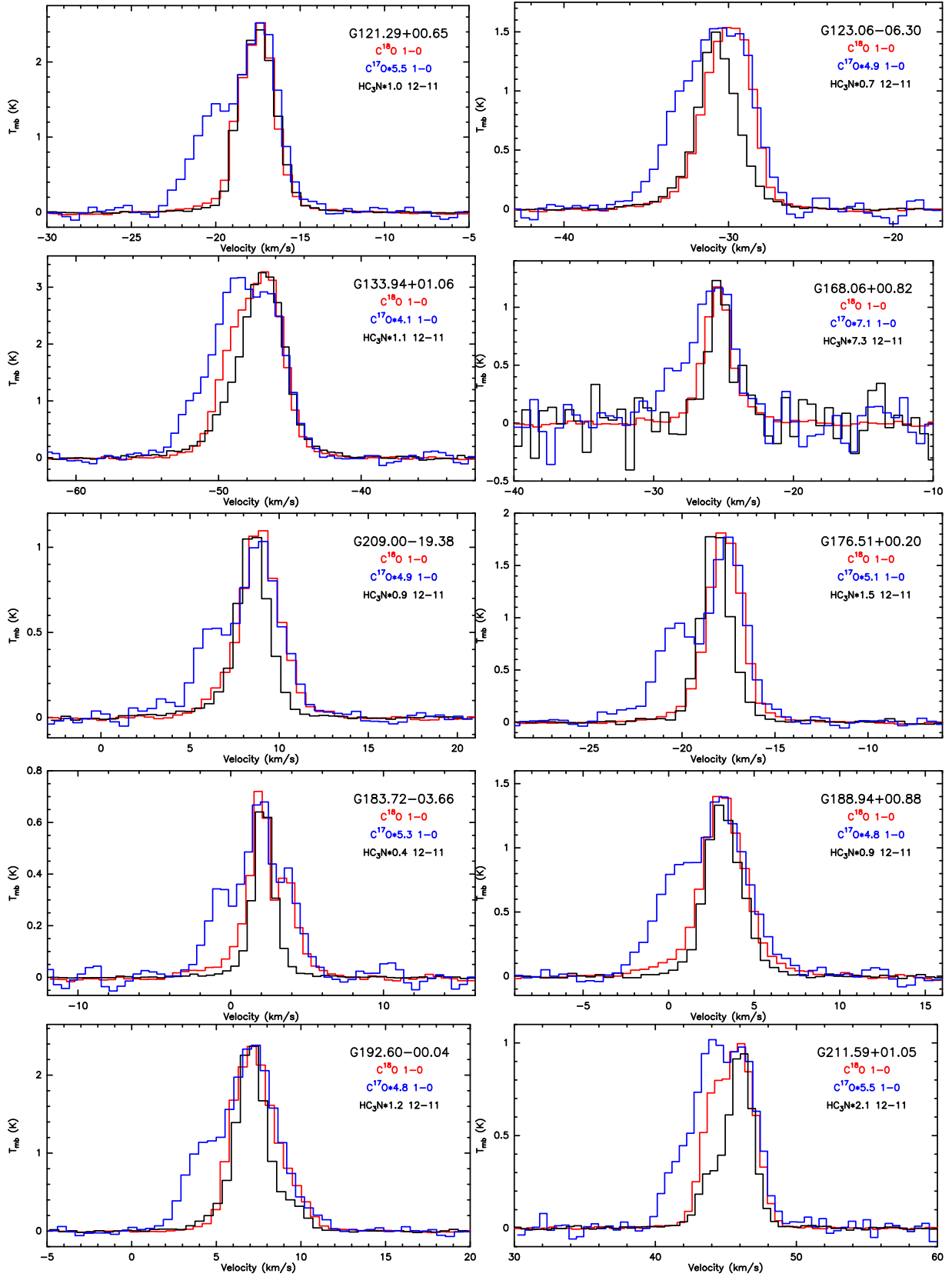


Figure A1. The observational results of spectra for  $C^{18}O$  1-0,  $C^{17}O$  1-0 and  $HC_3N$  12-11.

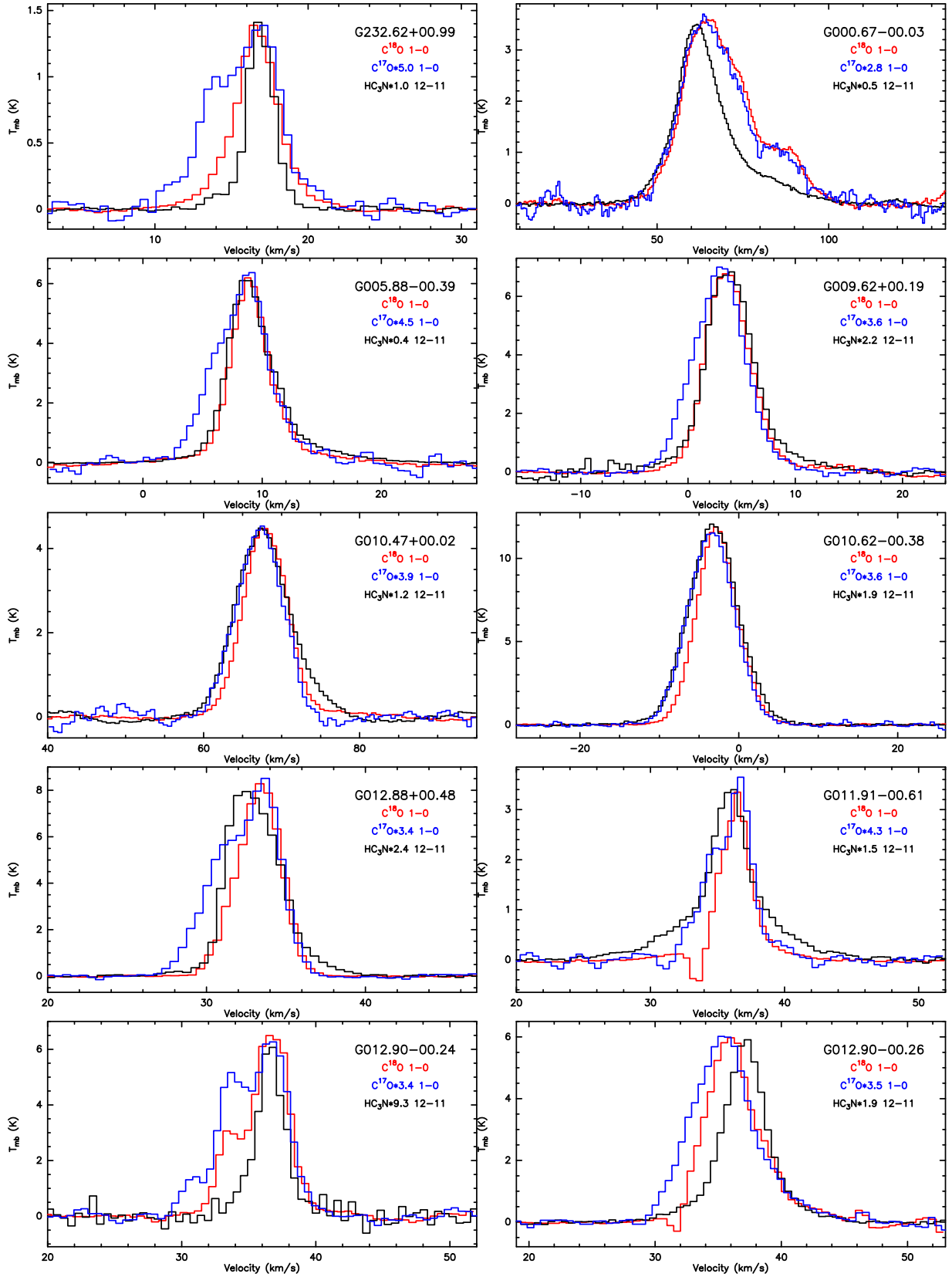


Figure A1. Continued.

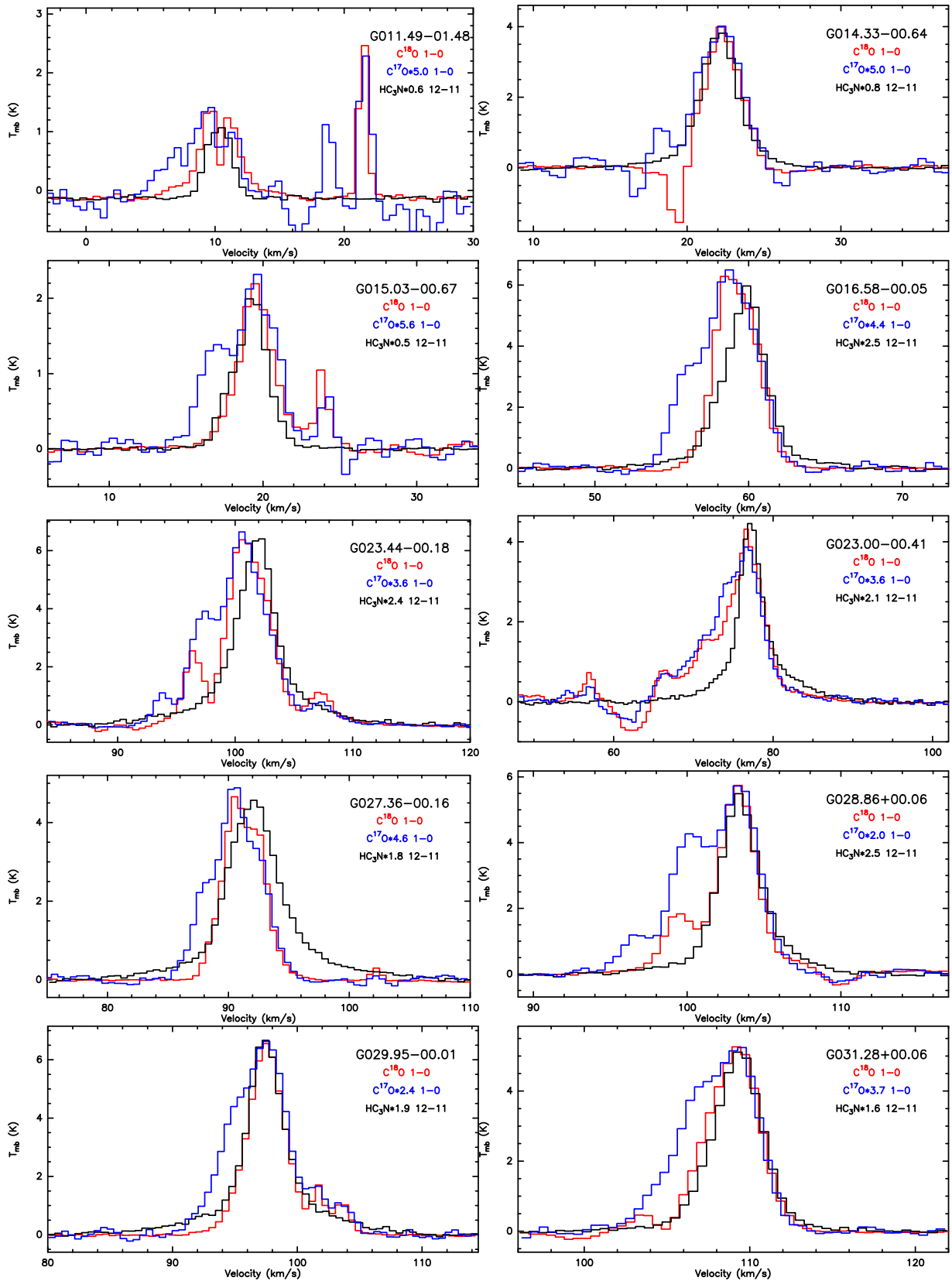


Figure A1. Continued.

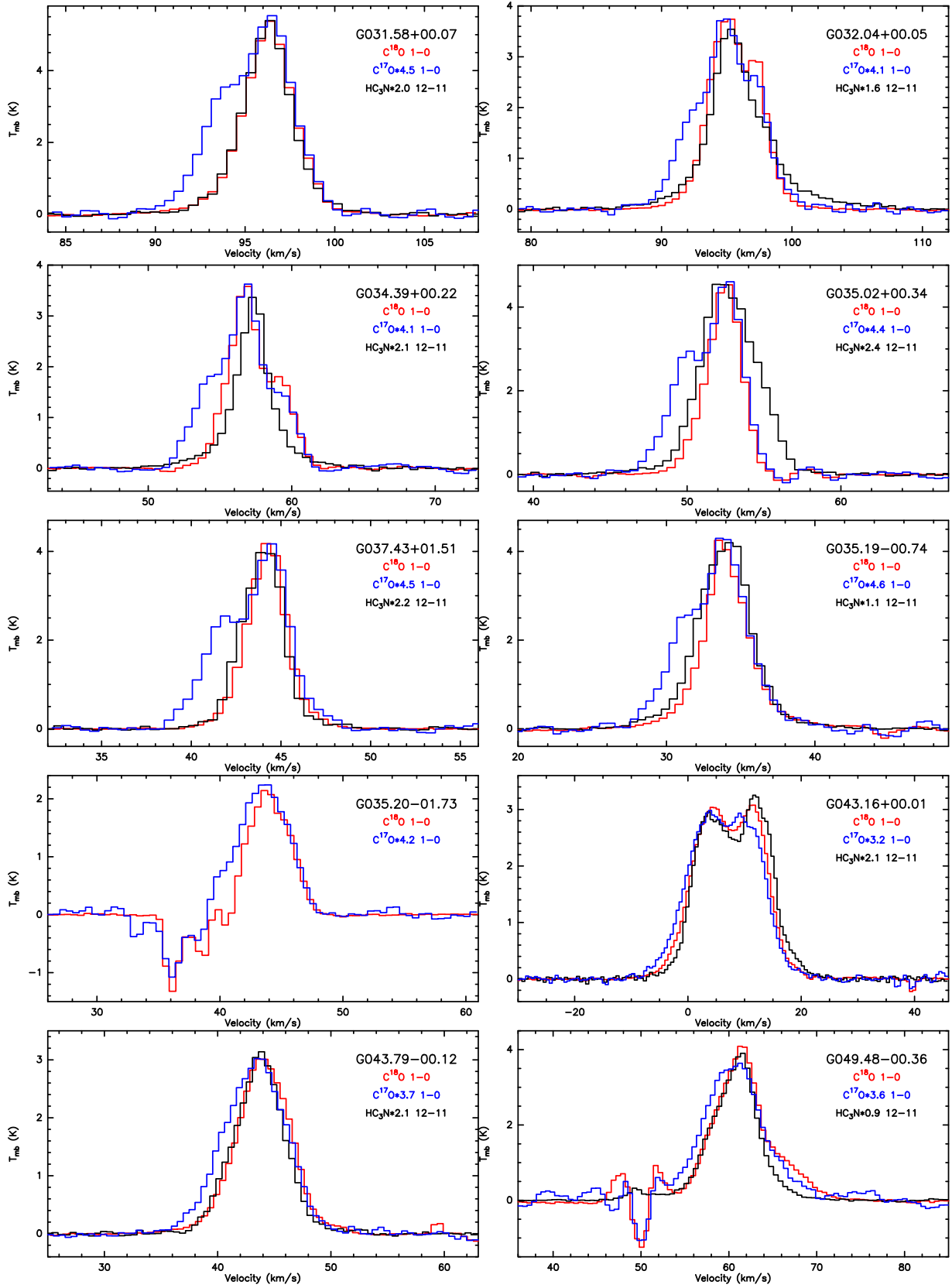


Figure A1. Continued.

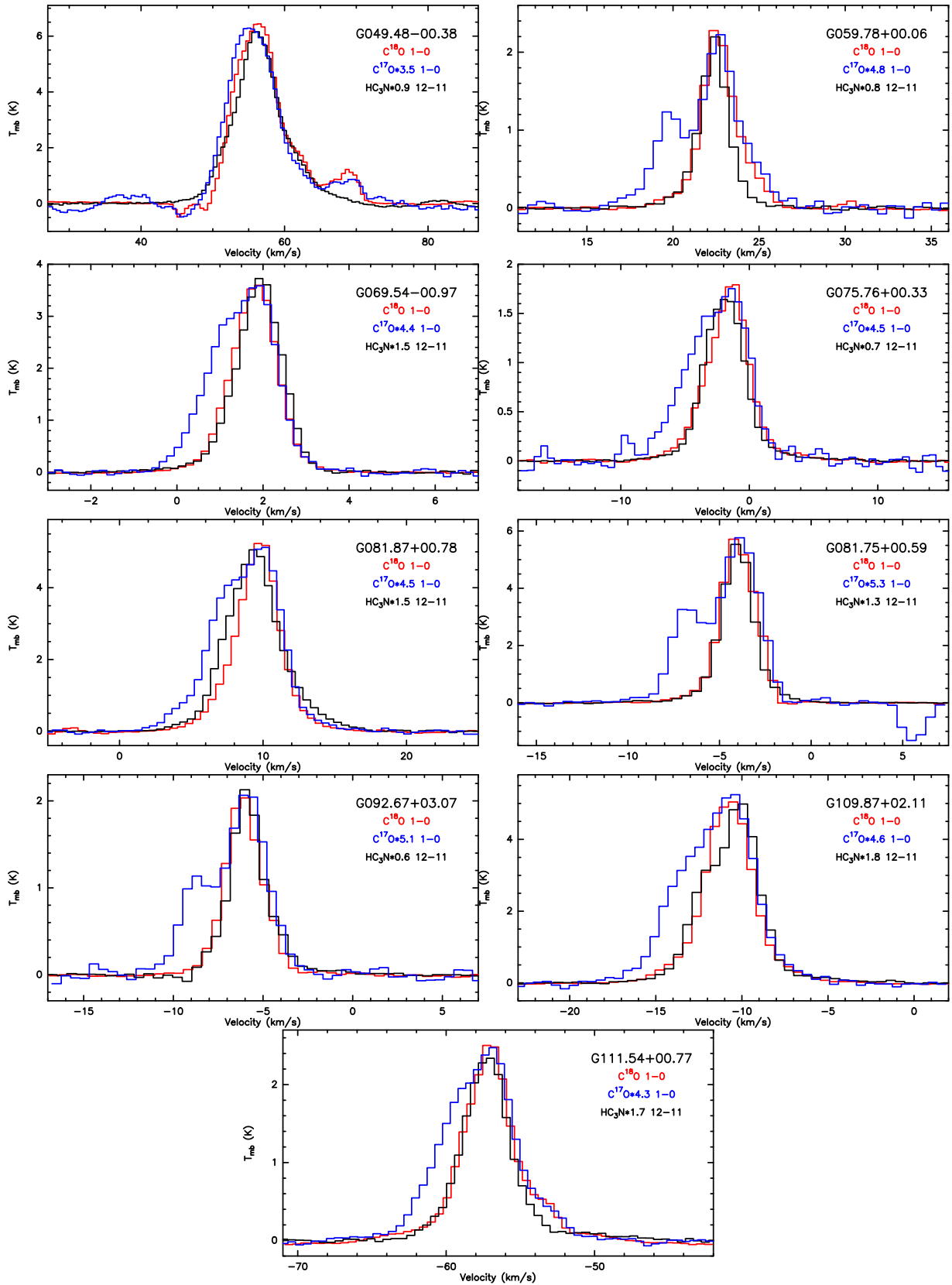
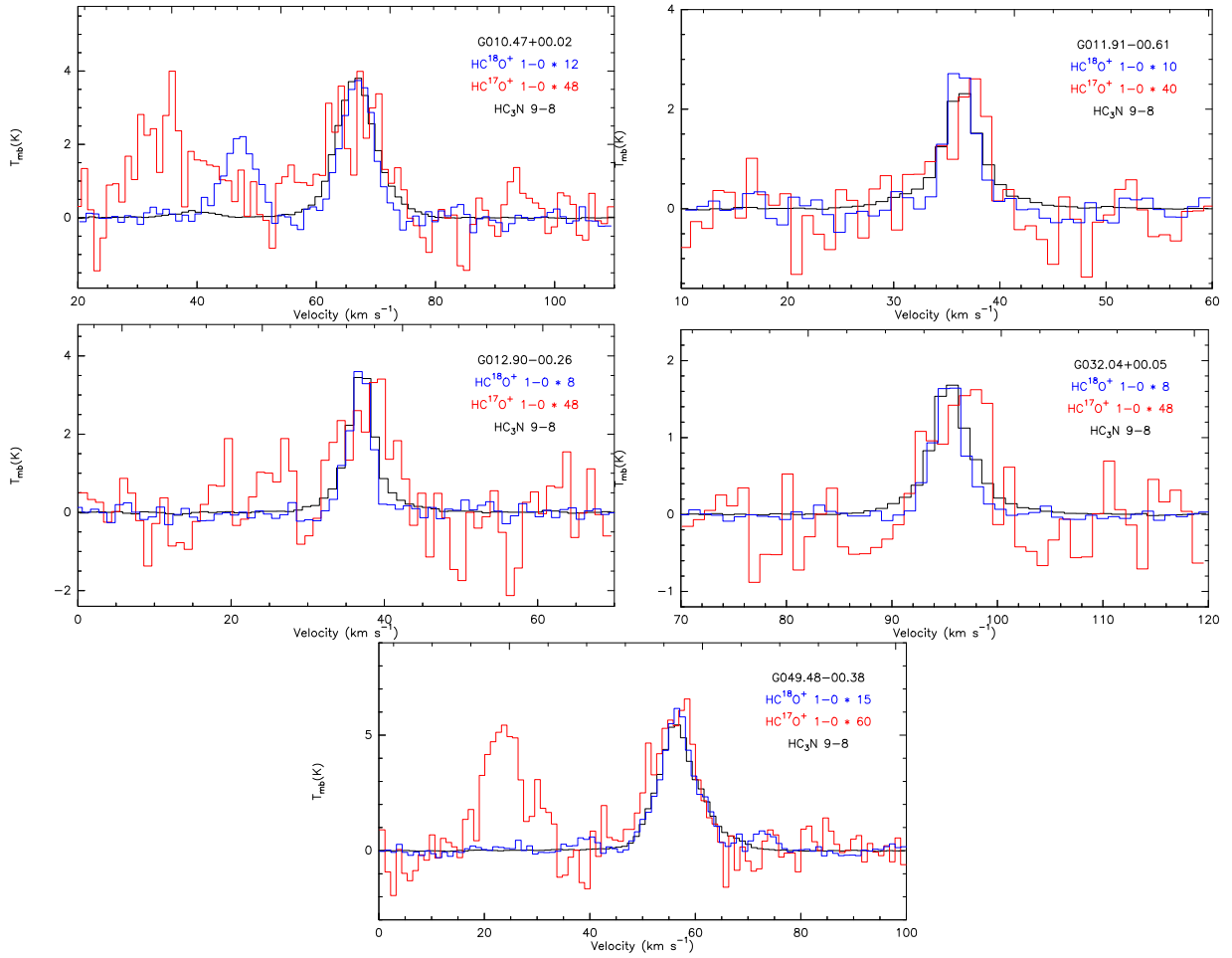


Figure A1. Continued.



**Figure A2.** The observational results of spectra for  $HC^{18}O^+$  1-0,  $HC^{17}O^+$  1-0 and  $HC_3N$  9-8.